DOI: https://doi.org/10.1080/10402004.2020.1717702

Flexible Support for Gas Lubricated Bearing Bushings

Philipp Bättig, Jürg Schiffmann

Ecole Polytechnique Fédérale de Lausanne, Laboratory for Applied Mechanical Design, Maladière 71b, CP 526, CH-2002 Neuchâtel 2

ABSTRACT

Herringbone-grooved journal bearings (HGJBs) for high speed turbo-machinery are often supported on O-Rings due to their favorable stiffness and damping characteristics for stability and alignment reasons. They yield, however, limited lifetime at high temperatures, insufficient assembly repeatability and dynamic characteristics that are difficult to measure and to tune. In order to overcome these shortcomings, a parametric model has been developed with the aim to design a flexible membrane bushing support that offers tunable tilting and radial stiffness and that can be coupled to various concepts to provide suitable damping levels to support a gas lubricated bearing bushing. Three damping concepts have been investigated that offer independent tuning of the support damping coefficient in combination with the novel flexible bearing bushing support. The new flexible membrane support was manufactured and its stiffness in radial and tilting direction measured before it was successfully implemented into a prototype.

Test results obtained from the new prototype with membrane support show a significant improvement in bushing alignment quality compared to O-Rings as well as stable operation up to the design rotor speed of 250 krpm.

KEYWORDS

Herringbone-grooved journal bearing; Flexible support; External damping; Stability threshold; High-speed turbo-machinery

INTRODUCTION

Gas lubricated bearings generally require very small clearances to allow stable rotor operation [1]. The consequences are high manufacturing costs, stringent misalignment tolerances and increased specific windage losses. Increased clearances are possible if the loss of rotordynamic performance is compensated through the addition of external damping [2]. External damping can be introduced either through squeeze film dampers [3, 4] or by flexibly mounting the bushings on soft supports [5, 6]. A commonly used procedure to stabilize the bearings and to therefore enable increased bearing clearances is to add external damping by supporting the bearing bushings on O-Rings [2, 7, 8]. The level of stiffness and damping of the flexible support determines the stability threshold

of the rotor-bearing system and/or the potential gain in bearing clearance. Other practical implementations of flexible elements to support herringbone-grooved journal bearings have been presented by Somaya et al. [5] and Yoshimoto et al. [6]. The solution presented by Somaya et al. provides a flexible support as well as Coulomb damping due to friction at the contact points of a flexible wire mesh, whereas Yoshimoto et al. support the bearing sleeve by three- or four-layered foils containing hemispherical bumps, similar to bump foils used in foil bearings. Both solutions, however, seem to be challenging in terms of bearing bushing alignment, tuning of the stiffness and damping characteristics and appear to be prone to a variation in stiffness and damping with age.

Nature of the issue

The use of O-Rings as a means to flexibly support bearing bushings of HGJBs offers various advantages such as low cost, ease of availability, compactness and favorable damping properties. Limited lifetime at high temperatures [9], insufficient assembly repeatability [10] and dynamic characteristics that are difficult to measure and to tune due to their dependency on many variables such as geometry, squeeze, material, loading type, temperature, frequency, vibration amplitude and age, make a reliable and reproducible implementation into products

challenging. The unfavorable repeatability of alignment is caused by twisted or nonplanarly fitted O-Rings during assembly and due to the typical O-Ring tolerance of 0.02 mm, which corresponds to about three times the radial clearance of a typical HGJB. Fig.1 demonstrates the insufficient repeatability of O-Ring supported bearing bushings by presenting measurements of the total rotor friction torque as a function of rotor speed obtained through coast-down tests of a gas bearing (HGJB) supported rotor with flexibly mounted bushings on O-Rings. All measurement sets were obtained from the same prototype using the same shaft on identical O-Ring supported bearing bushings. The rotor speed with the lowest total rotor friction torque can be associated to the bearing lift-off speed. The difference in the presented measurement results stems only from disassembly and reassembly of the shaft and/or bearing bushings. Since all the mechanical parts (rotor, bearing bushings, O-Rings) are identical, the results suggest that the difference in the measured friction torque is caused solely by the quality of the bearing bushing alignment. Misaligned bearing bushings cause increased low-speed frictional torque and non-repeatable lift-off speeds which can lead to increased losses and wear on bushings and rotor. A typical wear mark (wear dust accumulation in the bearing grooves) caused by O-Ring induced bushing misalignment is presented in Fig.2. These results clearly suggest that O-Rings do

not offer a repeatable and reliable means to flexibly support gas bearing bushings.

Goals and objectives

The objectives of this work are (1) to design an alternative flexible support based on the concept of thin membranes with parametric cutout geometries for HGJB bushings that offers independently tunable radial and tilting stiffness, (2) to verify the new support by commercial FEM software as well as measurements of radial and tilting stiffness, (3) to investigate various damping concepts that can be coupled to the new flexible bushing support and (4) to evaluate the performance of the novel flexible support in a prototype rotor running on HGJBs.

Scope of the Paper

The dynamic stiffness and damping characteristics of O-Rings currently used in a prototype are identified and serve as a baseline to develop an alternative flexible bearing bushing support. A parametric tool is developed that enables to predict the radial and tilting stiffness of membrane shaped disks. Monte-Carlo simulations are then performed to identify the design space offered by the developed flexible support. Various membranes are then manufactured and their radial and

tilting stiffness characterized and compared to commercial FEM software results as well as to the parametric membrane model presented in this paper. In order to complete the idea of an independently tunable flexible bearing bushing support, the performance of three damping concepts, compatible with the presented flexible support, is evaluated experimentally. The new flexible membrane support is then integrated into the baseline prototype and its performance assessed by means of coast-down and high-speed measurements.

METHODOLOGY

Setup for stiffness and damping measurements of flexible support

In order to characterize the dynamic properties of O-Rings and other flexible elements used to support gas bearing bushing a test rig has been designed based on the Base Excitation - Resonant Mass Method (BERM) [11]. A schematic diagram of the modular experimental setup is presented in Fig.3. In this test method a mass (1) is supported on a flexible element, in this case a pair of O-Rings (2), which are held in place in a housing (3) by means of exchangeable covers (4). The housing is mounted on an electromagnetic shaker (5). The mass and O-Rings therefore form a 2-DOF damped resonant system, which is excited by the vertical motion of the shaker. Measurement of the displacement of both

the housing and the supported mass using capacitance displacement probes (6) enables the determination of stiffness and damping coefficients of the flexible elements. The desired vibration frequency and amplitude are set using a waveform generator whose signals are fed to the shaker via an analog amplifier. The sensor signals of the capacitance displacement probes are amplified by means of a signal amplifier and then processed using LabVIEW. The modular experimental setup also allows to measure the dynamic characteristics of the flexible membrane support presented in this paper by adapting the test section, as shown in Fig.4. The test setup shown in Fig.3 and Fig.4 consists of a mass supported on two flexible elements which represents a 2-DOF system with a translational and a tilting vibration mode. Measurements using two proximity probes at each end of the supported mass were performed to ensure that the motion of the shaft is purely translational, hence the system can be treated as a 1-DOF system in the investigated frequency range. The response of a 1-DOF system shows a natural frequency which depends predominantly on the stiffness of the flexible elements and the supported mass. As described by Smalley et al. [11], accurate measurement data for stiffness and damping is restricted to the frequency range, where the phase angle difference between housing and supported mass is in the range of 15-165 deg. Taking this criteria into account, the natural frequency of the

spring-mass oscillator has to be tuned such that it is located within the frequency range of interest. The supported mass (element (1) in Fig.3) has been designed to tune the resonance frequency within 1500-4000 Hz, which is the typical range of the synchronous frequency for gas lubricated bearings. The vibration amplitude across the flexible elements was monitored using Eq.(1), which is valid for two sinusoidal signals of different amplitude but of identical frequency:

$$A_{fe} = 2\sqrt{A_1^2 + A_2^2 - 2A_1A_2\cos(\Delta\varphi)} \tag{1}$$

where A_{fe} is the amplitude across the flexible element, A_1 is the measured amplitude of the housing, A_2 is the amplitude of the supported mass and $\Delta\varphi$ is the phase angle difference between housing and supported mass.

The calculation of stiffness and damping for a 1-DOF model has been performed using Eq.(2) and Eq.(3) as presented by Gupta et al. [12]:

$$\frac{k_r}{m\omega^2} = \frac{\alpha(\alpha - \cos(\Delta\varphi))}{1 + \alpha(\alpha - 2\cos(\Delta\varphi))} \tag{2}$$

$$\frac{c}{m\omega} = \frac{\alpha\sin(\Delta\varphi)}{1 + \alpha(\alpha - 2\cos(\Delta\varphi))} \tag{3}$$

where k_r is the radial stiffness and c is the damping coefficient of the tested flexible elements, m the supported mass, ω the angular excitation frequency and α the amplitude ratio of supported mass and housing A_2/A_1.

Setup for performance evaluation of flexible support in prototype

The prototype used to investigate the new flexible bearing bushing support presented in this paper is shown in Fig.5. Due to the stiffness of the gas film, the orbital movement of the rotating shaft is transmitted to the flexibly supported bearing bushings. Any potential instability of the rotor-bearing-system can therefore be detected by measuring the motion of the bearing bushings, which is constantly monitored using two capacitance displacement probes per bearing bushing. The measurement data captured of the bearing bushing motion is analyzed by means of Fast-Fourier-Transformation (FFT) and the resulting frequency spectrum scanned for the presence of any sub-synchronous traces, which would indicate an instability of the rotor-bearing-system.

Table 2 lists all devices used to determine the dynamic characteristics of the novel flexible support presented in this paper, as well as the performance verification of the new flexible bearing bushing support in the prototype.

DEVELOPMENT OF ALTERNATIVE FLEXIBLE SUPPORT

Design requirements

The main requirements of the new flexible bearing bushing support are independently tunable radial and tilting stiffness and the option to add damping. Ideally,

the dynamic characteristics of a flexible support should be independent of excitation frequency, amplitude, temperature, age and other effects. Further prerequisites are a long lifetime ($\geq$ 4000 hours), minimal maintenance, low cost, as well as ease of manufacturing and implementation into existing prototypes and products. Additionally, the flexible bushing support needs to offer the possibility to perfectly align the bearing bushings. Theoretical investigations have shown the ideal support characteristics to be low radial stiffness, coupled with a high damping coefficient. However, too compliant supports potentially lead to large rotor orbits, which may cause a drop in turbomachinery performance due to the requirement of larger tip clearances [13, 14]. Table 3 summarizes the rotor and bearing configuration of the existing prototype, previously used with O-Rings to flexibly support the bearing bushings. Note that compared to the rotor diameter the bearing bushings are far apart, which makes the manufacturing of rigidly supported bushings challenging and expensive. Hence, a solution with flexibly supported and well-aligned bushings offers competitive advantages. This prototype serves as a baseline and is used to develop and test the new flexible bearing bushing support.

Parametric membrane model

Various concepts were evaluated with regards to the requirements presented above, which led to the selected solution being a membrane with cut-outs that can be easily manufactured by means of laser or water jet from a flat sheet of metal. The solid inner and outer ring sections are connected via flexible arms whose shapes are obtained by the specifically shaped cut-outs. The inner ring is connected to the bearing bushing, while the outer ring is connected to the machine housing. In order to predict the radial and tilting stiffness of such a flexible structure, a parametric model was developed. A sketch that illustrates the design variables of the flexible membrane model is presented in Fig.6. The design variables of the model include inner radius R_i, outer radius R_o, sector angle of one flexible element φ, the number of equally spaced annular sections n_{as}, the thickness t and width w of the flexible elements, the total number of flexible arms n_{fa} that form the complete flexible membrane structure, as well as the material to be used. In a first step, the shape of the flexible arm is determined by defining the angular location of a point on each of the equidistant annular sections. The points are then connected with a spline, which connects the inner and the outer ring. In order to predict the stiffness of such a structure, the flexible arms are modeled with finite elements along the spline. The shape of the spline

and the desired number of finite elements per spline n_{FE}, define the locations of the FE-nodes along the flexible arm, as represented by the red markers in step 2 of Fig.6. The 12x12 element stiffness matrices, offering three translational and three rotational degrees of freedom at each node, are defined between each pair of FE-nodes using Timoshenko's [15] beam theory, which includes both bending as well as shear effects. Each element stiffness matrix is first defined in local coordinates and then transformed in order to respect their global orientation along the spline, as presented in Eq.(4). $K_{el}^{'}$ represents the 12x12 stiffness matrix of the finite element in local coordinates, K_{el} the 12x12 stiffness matrix transformed into global coordinates, while T presents the direction transformation matrix. More detailed information about the mathematical modeling can be found in the APPENDIX.

$$K_{el} = T^T \cdot K_{el}^{'} \cdot T \tag{4}$$

The direction transformation is performed for all n_{FE} element stiffness matrices before they are assembled to form the $12n_{FE}$x$12n_{FE}$ stiffness matrix of one flexible arm K_{aba}. In order to reduce the calculation time, the $12n_{FE}$x$12n_{FE}$ stiffness matrix of the complete flexible arm K_{aba} is reduced to a 12x12 matrix offering six degrees of freedom at the inner node as well as six degrees of freedom at the outer node by means of the Guyan transformation [16]. The inner node connects

the flexible arm to the inner ring of the bushing support, while the outer node connects it to the outer ring of the bushing support. This procedure leads to the flexible arm being represented by an equivalent spring, as shown in step 2 of Fig.6, with six degrees of freedom at each end node. The reduced 12x12 stiffness matrix of one flexible arm K_a is determined according to Eq.(5), with T_{aba} being the Guyan transformation matrix.

$$K_a = {T_{aba}}^T \cdot K_{aba} \cdot T_{aba} \tag{5}$$

As shown in step 3 of Fig.6, the whole flexible membrane with n_{fa} flexible arms is constructed by assembling the n_{fa} 12x12 stiffness matrices K_a after transforming each of them with respect to their orientation in the global coordinate system, using the direction transformation as presented in Eq.(4). Note that the sector angle φ only serves to define the spline shape of the flexible arm and is not linked to the selected number of flexible arms n_{fa} for the whole flexible element, which can be freely chosen. The center points of inner and outer rings act as the master nodes, which are rigidly connected to the nodes where the flexible arms are attached, modeled by means of rigid body transformation. Master-Slave transformation, and binding the master node of the outer ring results in a 6x6 diagonal stiffness matrix whose values on the diagonal represent the translational stiffness in x-, y- and z-direction as well as the rotational stiffness around the x-, y- and

z-axis respectively. The translational stiffness in x- and y-direction represent the radial stiffness k_r, while the rotational stiffness in ϕ- and θ-direction represent the tilting stiffness k_t of the flexible membrane support. Due to symmetry reasons, the radial stiffness in x- and y-direction are identical, which is also the case for the tilting stiffness in ϕ- and θ-direction.

RESULTS AND DISCUSSION

Measurement of O-Ring stiffness and damping

Baseline values for stiffness and damping of the new flexible bearing bushing support are obtained by measurements performed on the silicone O-Rings currently used in the prototype with an internal diameter of 14 mm, a cross-sectional diameter of 1.5 mm, 1.43% stretch and 6.67% squeeze. Fig.7 presents the measurement results for radial stiffness k_r and damping coefficient c of a single silicone O-Ring obtained using the BERM method (refer to section METHODOLOGY) and the experimental setup shown in Fig.3. The vibration amplitude A_{fe} across the O-Rings was monitored during the tests and adjusted to 1 μm over the whole frequency range, which corresponds to typical operation of well balanced gas bearing supported high-speed rotors. The results suggest that the stiffness of the investigated O-Rings seems to increase with frequency, while the damping

coefficient decreases with increasing frequency. This corroborates results obtained by Smalley et al. [11], Tomioka et al. [17], Green et al. [18] and by Bättig and Schiffmann [19]. In the investigated frequency range of 1500-4500 Hz, the average radial stiffness for a single O-Ring is 5.5e+05 N/m, while the average damping coefficient is 6.16 Ns/m. Since each bearing bushing is supported on a pair of O-Rings, this leads to a baseline figure of k_r=1.1e+06 N/m and c=12.32 Ns/m for the new flexible membrane support.

Monte-Carlo simulations

In order to assess the design space of the parametric membrane support, three Monte-Carlo simulations have been performed for 500'000 membrane geometries made of PEEK, AL6082-T6 aluminum and 1.4310 stainless steel. The range of design variables used to perform the Monte-Carlo simulations is presented in Tab.4. Fig.8 presents the corresponding results of radial stiffness k_r against tilting stiffness k_t. The three points in the design space represent selected solutions of low, intermediate and high radial stiffness, whose shapes are shown in Fig.9. The results presented in Fig.8 suggest a possible design space ranging from 7e+00 N/m to 7e+09 N/m for the radial stiffness k_r, while the obtainable tilting stiffness k_t ranges from 6e-04 Nm/rad to 2e+06 Nm/rad, depending on

the selected material. Even though the investigated range of design variables is comparatively small, the results cover 9 orders of magnitude in radial and tilting stiffness, which offers a vast domain to select appropriate stiffness values. As suggested by Fig.9, the membrane design with the lowest stiffness (point 1) features four very long flexible arms. The stiffest solution (point 3) on the other hand, features the maximum amount of 12 straight radial elements. As can be observed in Fig.8, the upper and lower boundaries of the design space converge at its extremities of low and high radial stiffness, causing a reduction in the range of tunable tilting stiffness, while the center region of the design space (point 2) offers the largest range of selectable tilting stiffness for a given radial stiffness. For a given thickness t and width w, the stiffness of a flexible arm is predominantly governed by its length and shape. In theory, the softest possible solution features flexible arms that weave n_{as} times in alternating direction within the defined sector angle φ, whereas the theoretically stiffest solution is obtained by connecting the outer and inner radii covering the shortest possible distance, resulting in straight radial elements. For both of these two extreme cases, only one geometrical solution exists, which explains the convergence of the design space to a tip at both extremities. In the center section of the design space, however, an infinite amount of geometrical solutions exists, meaning that the flexible arms

can take any shape or length, resulting in a wide domain of results for the designer to choose from.

Model verification

The results of the parametric membrane tool were verified for various geometries using a commercial FEM software. A model using 1D beam elements as well as a 3D model using tetrahedral elements has been set up to determine the radial and tilting stiffness k_r and k_t. Fig.10 compares the displacements of the parametric membrane model presented in this paper with the results from 1D and 3D models obtained with the commercial FEM code for a radial force F_r of 1 N applied in the center of the membrane, corresponding to the maximum expected force acting on the membranes during operation. Evaluating the radial displacement for a given force applied to the center node of the membrane allows the determination of the radial stiffness k_r. The same procedure was followed to calculate the tilting stiffness k_t, where the angular displacement ϕ for a given tilting torque T in the center of the membrane was evaluated. Table 5 presents the radial and tilting stiffness k_r and k_t obtained with the parametric membrane model and compares them to the results from 1D and 3D FEM simulations. As suggested by Tab.5, the stiffness results obtained with the membrane model match

the 1D FEM results very well with a deviation of only 0.19% and 0.12% for radial stiffness k_r and tilting stiffness k_t respectively. Stiffness values obtained with the 3D FE model are 9.17% and 3.84% higher for radial and tilting stiffness compared to the 1D model, which is most likely caused by the different boundary conditions at the end of the flexible arms at the inner and at the outer radius. The comparison of the parametric reduced-order model and more sophisticated modeling approaches clearly show a good agreement.

Experimental verification

Radial stiffness measurements of three different membrane geometries were performed using the test rig shown in Fig.4. Two membranes were manufactured in aluminum AL6082-T6 and one in steel 1.4310, all laser cut starting from a precision metal sheet. The geometrical properties of all investigated membrane geometries are detailed in Fig.11 and Tab.1. Fig.12 presents the measured radial stiffness k_r for aluminum membrane Var20 and Var45 and steel membrane Var28 using the BERM method. The designed radial stiffness k_r for membrane Var20, Var45 and Var28 is 1.00e+06 N/m, 1.04e+06 N/m and 1.04e+06 N/m respectively. Averaging the measured radial stiffness k_r over the investigated frequency range results in 0.82e+06 N/m for membrane Var20, 0.92e+06 N/m for

membrane Var45 and 1.33e+06 N/m for membrane Var28. This corresponds to -18%, -11.5% and +27.9% for membranes Var20, Var45 and Var28 compared to the design values obtained by the parametric membrane model. Compared to O-Rings, whose dynamic characteristics are highly dependent on the excitation frequency [11, 18, 19, 20, 21], the membrane measurement results suggest that the radial stiffness k_r is independent of the excitation frequency f, which makes their use as a flexible support for HGJB bushings significantly easier and more predictable.

Smalley et al. [11] have investigated the effect of temperature on the stiffness and damping of O-Rings. They found the stiffness to decrease by a factor of 2 and the damping by a factor of 4 when increasing the temperature from 25 °C to 66 °C. In contrast, the elastic modulus for 1.4310 stainless steel and AL6082-T6 aluminum, which is the governing variable for the stiffness of the presented flexible membrane support, decreases by only 7% [22] and 0.8% [23] respectively in the temperature range up to 66 °C and by 17% and 8.5% respectively for a temperature increase up to 200 °C.

Measurements of the tilting stiffness k_t were performed on three different membranes. The designed tilting stiffness k_t is 5.1 Nm/rad, 35.2 Nm/rad and 64.8 Nm/rad for aluminum membrane Var19, steel membrane Var8 and Var23 respec-

tively. Fig.13 presents the measured angular displacement ϕ of the membrane center when a torque T is applied to the center of the flexible membrane. The applied tilting torque is varied by adding different weights to a bar that is fixed to the membrane center. The slope of a line fitted to the measurement results represents the tilting stiffness k_t for each membrane. As suggested by Fig.13, the measured tilting stiffness k_t is 4.3 Nm/rad, 21.8 Nm/rad and 28.3 Nm/rad for membranes Var19, Var8 and Var23 respectively. This corresponds to a difference of -16% for Var19, -38% for Var8 and -56% for Var23 compared to the predicted tilting stiffness k_t by the parametric membrane model.

The difference in predicted and measured radial and tilting stiffness has been identified to be caused by manufacturing errors during the laser-cutting process, which caused some membranes to have flexible arms of significantly different width w than designed. Fig.14 presents an overlay of the designed geometry and the real geometry achieved by laser cutting for membrane Var23, which presented the largest deviation of predicted and measured stiffness. Geometrical measurements performed on this membrane resulted in some flexible arms to be of only 0.3 mm in width w instead of the designed 0.524 mm. Using the parametric membrane model presented in this paper, the predicted tilting stiffness k_t for this membrane with flexible arms of 0.3 mm width w is 33.0 Nm/rad, re-

sulting in a deviation of only 14.2% between measurement and calculation. The radial stiffness k_r decreases to 0.21e+06 N/m, which represents a drop of 81%. The difference in designed and real geometry stems from incorrect compensation of the laser beam radius as well as thermal deflection due to the heat input during the laser cutting process. The results suggest that aluminum membranes suffer less from this effect, most probably due to the significantly higher thermal conductivity of aluminum compared to stainless steel. The manufacturing errors caused by thermal distortion during the cutting process could be further reduced using water-jet or wire-erosion technology.

Damping concepts

Three damping concepts have been studied that can be combined with the presented flexible membrane support. The three investigated concepts are presented in Fig.15 and consist of a silicon coating, a friction disk and a membrane stack. Subfigure a) in Fig.15 presents the silicone coating concept (Sil), where a membrane is dipped into liquid SS-101 silicone and then left to rest for the silicone to solidify. b) presents the friction disk concept (FD), which consists of an axially preloaded friction disk rubbing on a polymer ring that is fixed to the flexible membrane support. The relative motion between friction disk and polymer ring

causes a radial friction force, which induces damping, that can be tuned either by a variation of the axial preload between the friction disc and the flexible membrane, or by the friction coefficient. The third damping concept presented in c) consists of a stack of three membranes, each one 1/3 of the thickness t of the regular membrane, resulting in an identical radial stiffness as the regular membrane. The membrane stack (MS) is constructed by stacking three membranes in alternating direction, in order to generate friction between the flexible arms, which leads to Coulomb damping. The damping concepts silicone coating (Sil) and membrane stack (MS) present a coupling effect between the membrane design and the resulting damping, since the damping is a result of the motion of the flexible arms. In the case of the friction disk concept (FD), the damping is governed primarily by the friction between the friction disk and the bushing. Hence, the stiffness and the damping can be considered as coupled in parallel with a minimal coupling effect between the membrane design and the resulting damping.

The effectiveness of the three presented damping concepts was investigated using the same setup as presented in section METHODOLOGY. Fitting the response of a 1-DOF spring-damper system to the measurement data allows the identification of an equivalent damping coefficient c for the presented damping

concepts. The bar plot in Fig.16 presents the determined equivalent damping coefficient c for membranes Var45 with/without silicone coating (Sil), Var20 with/without friction disk (FD), as well as for membrane Var28 as a single membrane compared to a membrane stack (MS). The dashed line represents the average damping coefficient of the previously used pair of silicone O-Rings, as presented in Fig.7. As suggested by Fig.16, the silicone coating (Sil) increases the damping coefficient c of membrane Var45 by 125%, while the friction disk concept (FD) increases the damping coefficient c of membrane Var20 by 400%. The results suggest that the membrane stack damping concept (MS) offers the highest potential to increase damping. Replacing membrane Var28 by a membrane stack of three identical membranes with 1/3 of the thickness increases the damping coefficient c by 860%. Furthermore, the results suggest that all three investigated damping concepts offer damping coefficients in the same order of magnitude as the previously measured pair of O-Rings, which makes them viable candidates to be coupled with the flexible membrane support.

Safety against fatigue failure

The membrane version to be implemented in the prototype is Var6 (see geometrical details in Fig.11 and Tab.1), whose radial stiffness of k_r=1.1e+06 N/m is

identical to the previously used pair of O-Rings. The membranes are laser-cut from an AL6082-T6 precision aluminum sheet. The fatigue strength of the flexible membrane support has been evaluated by comparing the maximum von-Mises stress, caused by a radial vibration amplitude of 5 μm, with measured fatigue data of AL6082-T6. The FEM predicted maximum von-Mises stress is σ_a=17.85 MPa. Karolczuk et al. [24] present experimental fatigue failure data for AL6082-T6 in pure cyclic bending, which allows to predict the expected cycles to failure according to Eq.(6).

$$log_{10}(N_f) = 23.8 - 8log_{10}(\sigma_a) \tag{6}$$

For a predicted stress amplitude of σ_a=17.85 MPa, the expected cycles to failure is N_f=6.12e+13, according to Eq.(6). Assuming a 4000 hour service life at a design rotor speed of 250 krpm, resulting in 6e+10 cycles before failure, the safety factor for life is therefore s_l=1.02e+03. Evaluation of Eq.(6) for the required 6e+10 cycles allows to calculate the maximum allowed stress amplitude for the structure to not fail before the required number of cycles and results in σ_{max}=42.44 MPa. The ratio of maximum allowed stress amplitude σ_{max} and predicted stress amplitude σ_a represents a safety factor for stress of $s_\sigma = 2.4$. Both safety factors show a sufficiently high margin against fatigue failure, suggesting unlimited endurance for the introduced flexible bearing support concept.

Implementation into prototype and testing

In order to ensure perfect alignment of the two flexibly supported bearing bushings, concentricity to the motor axis, as well as perpendicularity of the bushing axes to the thrust bearing surface, a special procedure is used to align the front and back bearing bushings in their respective flexible membranes. The procedure consists in aligning the bushings on a high precision assembly shaft with minimal clearance that is mounted on the prototype and serves to position the bushings within the machine. The membranes are fixed on their outer diameter (OD) to the machine body using a clamp ring and bolts. The membrane inner diameter (ID) is designed such that an assembly gap forms between the OD of the bearing bushing and the membrane ID, which is then filled with glue. After curing of the glue, the assembly shaft is removed and replaced with the real rotor. Fig.17 presents the aligned and glued front bearing bushing fastened to the main housing using a clamp ring and bolts.

Fig.18 presents four coast-down measurements from 50 krpm to 0 krpm obtained from the new prototype with bearing bushings supported on flexible membranes as pictured in Fig.5. The presented measurement results stem from an identical prototype using the same shaft on identical membrane supported bearing bushings and were obtained after disassembly and reassembly of the shaft and/or

bearing bushings for inspection. The results in Fig.18 suggest that the total rotor friction torque and therefore the alignment of the bushings is unaffected by operational time and is reproducible after dis-assembly and re-assembly of the prototype. Compared to the situation with the O-Ring supported bushings, the membrane solution together with the assembly procedure allows to improve the repeatability of the assembly significantly.

Due to the stiffness of the gas film, the orbital movement of the rotating shaft is transmitted to the flexibly supported bearing bushings. Any potential instability of the rotor-bearing-system can therefore be detected by measuring the motion of the bearing bushings. Fig.19 presents the waterfall plot from the measured bushing motion during a speed ramp from 0 to 250 krpm of the new prototype supported on flexible membranes. The absence of any sub-synchronous vibrations in the waterfall plots of Fig.19 suggests stable operation of the prototype up to 250 krpm. Fig.20 presents the evolution of synchronous motion amplitudes of front and back bearing bushings of the new prototype during acceleration of the rotor from standstill to its design rotor speed of 250 krpm. The measurements suggest motion amplitudes peaking at 1 μm, corroborating the assumed radial force F_r of 1 N for the determination of the stiffness of the presented membrane geometries, which offer a radial stiffness k_r of about 1 N/μm. Furthermore, the

observed maximum motion amplitudes of 1 μm are lower than the assumed amplitude of 5 μm that was assumed for the fatigue failure assessment, suggesting the safety factors for fatigue failure to be even higher than predicted.

SUMMARY AND CONCLUSION

In this paper, a flexible support concept for HGJB bushings is presented that allows to independently vary radial and tilting stiffness and that can be coupled to various measures to include damping. The presented flexible support is easy and cheap to manufacture, offers dynamic characteristics that are largely independent of excitation frequency, temperature, age and offers a wide range of support stiffnesses (9 orders of magnitude) that enables the designer to choose the optimum characteristics depending on the application. The parametric model developed in this paper enables to quickly and accurately predict the radial and tilting stiffness of the novel flexible support. Furthermore, three damping concepts are presented that offer independently tunable damping coefficient and that can be coupled to the flexible membrane support.

High-speed measurements have been performed up to 250 krpm and no signs of rotor instability was detected. The measured synchronous bushing motion amplitudes peak at 1 μm. A fatigue failure investigation clearly suggests that

the stress level induced by the rotor motion is sufficiently low to achieve unlimited endurance. Furthermore, the measurement results of the new flexible bearing support suggest very good bushing alignment that is unaffected by assembly/disassembly and operational time. As a consequence, the introduced support concept offers an easy to implement solution to introduce flexible and tunable support for fluid film bearings.

ACKNOWLEDGMENT

The authors acknowledge the co-funding by the Swiss National Science Foundation, grant PYAPP2_154278/1. The authors have no conflict of interest to declare.

References

[1] J. Schiffmann, "Enhanced groove geometry for herringbone grooved journal bearings," *Journal of Engineering for Gas Turbines and Power*, vol. 135, p. 102501, October 2013.

[2] G. Belforte, F. Colombo, T. Raparelli, and V. Viktorov, "High-speed rotor with air bearings mounted on flexible supports: test bench and experimental results," *Journal of Tribology*, vol. 130, p. 021103, 2008.

[3] A. Szeri, A. Raimondi, and A. Giron-Duarte, "Linear force coefficients for squeeze-film dampers," *Journal of Lubrication Technology*, vol. 105, no. 3, pp. 326–334, 1983.

[4] F. Y. Zeidan, L. S. Andres, and J. Vance, "Design and application of squeeze film dampers in rotating machinery," in *Proceedings of the 25th Turbomachinery Symposium*, (Houston, Texas, USA), pp. 169–188, Sept 17-19 1996.

[5] K. Somaya, M. Miyatake, K. Okubo, and S. Yoshimoto, "Threshold speed of instability of a herringbone-grooved rigid rotor with a bearing bush flexibly supported by straight spring wires," in *Proceedings of ASME*

Turbo Expo 2015: Turbine Technical Conference and Exposition GT2015, vol. 7A, (Montreal, Canada), p. V07AT31A015, June 15–19 2015.

[6] S. Yoshimoto, M. Miyatake, and K. Nagata, "Instability of herringbone grooved aerodynamic floating bush bearings flexibly supported by foils with hemispherical bumps," in *Proceedings of ASME/STLE International Joint tribology Conference*, (San Diego, California, USA), pp. 261–263, 10 2007.

[7] T. Waumans, J. Peirs, F. Al-Bender, and D. Reynaerts, "Aerodynamic journal bearing with a flexible, damped support operating at 7.2 million dn," *Journal of Micromechanics and Microengineering*, vol. 21, p. 104014, September 2011.

[8] N. Miyanaga and J. Tomioka, "Effect of support stiffness and damping on stability characteristics of herringbone-grooved aerodynamic journal bearings mounted on viscoelastic supports," *Tribology International*, vol. 100, pp. 195–203, August 2016.

[9] M. Darlow and E. Zorzi, "Mechanical design handbook for elastomers," Tech. Rep. Contractor Report 3423, Mechanical Technology Incorporated, NASA Lewis Research Center, 1981.

[10] I. Green and C. English, "Analysis of elastomeric o-ring seals in compression using the finite element method," *Tribology Transactions*, vol. 35, no. 1, pp. 83–88, 1992.

[11] A. Smalley, M. Darlow, and R. Mehta, "The dynamic characteristics of o-rings," *Journal of Mechanical Design*, vol. 100, pp. 132–138, January 1978.

[12] P. Gupta, J. Tessarzik, and L. Cziglenyi, "Development of procedures for calculating stiffness and damping properties of elastomers in engineering applications - part ii: Elastomer characteristics at constant temperature," Technical report CR-134704, Mechanical Technology Incorporated, NASA Lewis Research Center, April 1974.

[13] R. Pampreen, "Small turbomachinery compressor and fan aerodynamics," *Journal of Engineering for Gas Turbines and Power*, vol. 95, pp. 251–256, July 1973.

[14] J. J. Brasz, "Investigation into the effect of tip clearance on centrifugal compressor performance," in *ASME 1988 International Gas Turbine and Aeroengine Congress and Exposition*, vol. 1, (Amsterdam, Netherlands), p. V001T01A066, ASME, June 6-9 1988.

[15] S. Timoshenko and J. Gere, *Theory Of Elastic Stability*. Dover Civil and Mechanical Engineering, Dover Publications, 2 ed., 2012.

[16] R. Guyan, "Reduction of stiffness and mass matrices," *American Institute of Aeronautics and Astronautics*, vol. 3, no. 2, pp. 380–380, 1965.

[17] J. Tomioka and N. Miyanaga, "Measurement of dynamic properties of o-rings and stability threshold of flexibly supported herringbone grooved aerodynamic journal bearings," *Tribology Online*, vol. 3, no. 7, pp. 366–369, 2008.

[18] I. Green and I. Etsion, "Pressure and squeeze effects on the dynamic characteristics of elastomer o-rings under small reciprocating motion," *Journal of Tribology*, vol. 108, pp. 439–444, July 1986.

[19] P. Bättig and J. Schiffmann, "Data-driven model for the dynamic characteristics of o-rings for gas bearing supported rotors," *Journal of Applied Mechanics*, vol. 86, no. 8, p. 081003, 2019.

[20] T. Shoyama and K. Fujimoto, "Calculation of high-frequency dynamic properties of squeezed o-ring for bearing support," *Mechanical Engineering Journal*, vol. 5, no. 2, pp. 17–00444, 2018.

[21] J. Yan, Y. Wang, S. Wang, and X. Su, "Frequency dependence stiffness and damping of o rubber ring," *Advanced Materials Research*, vol. 904, pp. 368–372, May 2014.

[22] Zapp Precision Metals GmbH, Unna, Germany, *Stainless Spring Steel Strip Zapp 1.4310*, February 2018.

[23] N. Torić, J. Brnić, I. Boko, M. Brčić, I. W. Burgess, and I. Uzelac, "Experimental analysis of the behaviour of aluminium alloy en 6082aw t6 at high temperature," *Metals*, vol. 7, p. 126, April 2017.

[24] A. Karolczuk, M. Kurek, and T. Lagoda, "Fatigue life of aluminium alloy 6082 t6 under constant and variable amplitude bending with torsion," *Jounal of Theoretical and Applied Mechanics*, vol. 53, no. 2, pp. 421–430, 2015.

[25] T. Gmür, *Méthode des éléments finis*. Presses polytechniques et universitaires romandes, 2007.

APPENDIX - Details of mathematical modeling

The 12x12 element stiffness matrix $K_{el}^{'}$ for each finite element in local coordinates is constructed according to Timoshenko [15], with w being the width, t the thickness, l the length, E the Young's modulus and G the shear modulus of the finite element.

$$I = \frac{1}{12}\begin{pmatrix} 4wt^3 \\ wt^3 \\ w^3t \end{pmatrix} \quad c = \frac{12E}{Gwtl^2}\begin{pmatrix} 0 \\ 1.2I_3 \\ 1.2I_3 \end{pmatrix} \tag{7}$$

$$a = \begin{pmatrix} \frac{Ewt}{l} \\ \frac{GI_1}{l} \\ \frac{12EI_3}{l^3(1+c_2)} \\ \frac{6EI_3}{l^2(1+c_2)} \\ \frac{EI_3}{l}\frac{4+c_2}{1+c_2} \\ \frac{EI_3}{l}\frac{2-c_2}{1+c_2} \\ \frac{12EI_2}{l^3(1+c_3)} \\ \frac{6EI_2}{l^2(1+c_3)} \\ \frac{EI_2}{l}\frac{4+c_3}{1+c_3} \\ \frac{EI_2}{l}\frac{2-c_3}{1+c_3} \end{pmatrix} \tag{8}$$

$$K_{el}^{'} = \begin{bmatrix} a_1 & 0 & 0 & 0 & 0 & 0 & -a_1 & 0 & 0 & 0 & 0 & 0 \\ 0 & a_3 & 0 & 0 & 0 & a_4 & 0 & -a_3 & 0 & 0 & 0 & a_4 \\ 0 & 0 & a_7 & 0 & -a_8 & 0 & 0 & 0 & -a_7 & 0 & -a_8 & 0 \\ 0 & 0 & 0 & a_2 & 0 & 0 & 0 & 0 & 0 & -a_2 & 0 & 0 \\ 0 & 0 & -a_8 & 0 & a_9 & 0 & 0 & 0 & a_8 & 0 & a_{10} & 0 \\ 0 & a_4 & 0 & 0 & 0 & a_5 & 0 & -a_4 & 0 & 0 & 0 & a_6 \\ -a_1 & 0 & 0 & 0 & 0 & 0 & a_1 & 0 & 0 & 0 & 0 & 0 \\ 0 & -a_3 & 0 & 0 & 0 & -a_4 & 0 & a_3 & 0 & 0 & 0 & -a_4 \\ 0 & 0 & -a_7 & 0 & a_8 & 0 & 0 & 0 & a_7 & 0 & a_8 & 0 \\ 0 & 0 & 0 & -a_2 & 0 & 0 & 0 & 0 & 0 & a_2 & 0 & 0 \\ 0 & 0 & -a_8 & 0 & a_{10} & 0 & 0 & 0 & a_8 & 0 & a_9 & 0 \\ 0 & a_4 & 0 & 0 & 0 & a_6 & 0 & -a_4 & 0 & 0 & 0 & a_5 \end{bmatrix} \tag{9}$$

The direction transformation of one single element stiffness matrix $K_{el}^{'}$ from local coordinates into global coordinates is presented in Eq.(10).

$$K_{el} = T^T \cdot K_{el}^{'} \cdot T \tag{10}$$

The direction transformation matrix T for a rotation φ around the z-axis is given in Eq.(11), with φ being the angle of the finite beam element with respect to the

x-axis of the global coordinate system.

$$T_{sub} = \begin{bmatrix} cos(\varphi) & sin(\varphi) & 0 \\ sin(\varphi) & -cos(\varphi) & 0 \\ 0 & 0 & 1 \end{bmatrix} \qquad T = \begin{bmatrix} T_{sub} & 0 & 0 & 0 \\ 0 & T_{sub} & 0 & 0 \\ 0 & 0 & T_{sub} & 0 \\ 0 & 0 & 0 & T_{sub} \end{bmatrix} \tag{11}$$

The transformed 12x12 element stiffness matrices K_{el} are assembled according to the classical Finite-Element theory to form the $12n_{FE}$x$12n_{FE}$ stiffness matrix of one flexible arm K_{aba}, as shown in Eq.(12), where A represents the matrix assembly operator [25].

$$K_{aba} = A_{i=1}^{n_{FE}} K_{el_i} \tag{12}$$

The reduction of the large K_{aba} matrix into a reduced form, which only features the degrees of freedom at the inner and the outer node, is performed by means of the Guyan transformation [16]. The definition of the Guyan transformation matrix T_{aba}, which is used to express all degrees of freedom, q_a and q_b, by only the preferential degrees of freedom q_a, is presented in Eq.(13):

$$\begin{pmatrix} q_a \\ q_b \end{pmatrix} = T_{aba} \cdot q_a \tag{13}$$

The definition of matrix T_{aba} is given in Eq.(14), where T_{aa} is an identity matrix of dimension 12x12, that is used to transform the 12 preferential degrees

of freedom into itself, while T_{ba} is used to transform the preferential degrees of freedom q_a into the non-preferential ones q_b.

$$T_{aba} = \begin{pmatrix} T_{aa} \\ \\ T_{ba} \end{pmatrix} \tag{14}$$

The matrix T_{ba} is defined according to Eq.(15), where K_{bb} and K_{ba} are sub-matrices of the original stiffness matrix K_{aba} with respect to the preferential and non-preferential degrees of freedom, as shown in Eq.(16).

$$T_{ba} = -{K_{bb}}^{-1} \cdot K_{ba} \tag{15}$$

$$K_{aba} = \begin{bmatrix} K_{aa} & K_{ab} \\ \\ K_{ba} & K_{bb} \end{bmatrix} \tag{16}$$

Nomenclature

Roman symbols

A	Vibration amplitude, [m]
c	Damping coefficient, [Ns/m]
D	Diameter, [m]
E	Young's modulus, [Pa]
f	Frequency, [Hz]
G	Shear modulus, [Pa]
I	Area moment of inertia, [m^4]
J	Inertia, [kgm^2]
K	Stiffness matrix, [N/m]
k	Stiffness, [N/m]
l	Length, [m]
m	Mass, [kg]
N	Rotational speed, [1/min]
N	Number of cycles, [-]
n	Number of, [-]
q	Translation, [m]
R	Radius, [m]

s	Safety factor, [-]
T	Transformation matrix
T	Torque, [Nm]
t	Thickness, [m]
w	Width, [m]

Greek symbols

α	Amplitude ratio $\frac{A_2}{A_1}$, [-]
$\Delta\varphi$	Phase angle difference, [rad]
θ	Angular displacement, [rad]
μ	Poisson ratio, [-]
ρ	Density, [kg/m^3]
σ	Stress, [MPa]
Φ	Angular displacement, [rad]
φ	Sector angle, [rad]
ω	Angular frequency, [rad/s]

Subscripts

1	Housing
2	Mass
a	Preferential
b	Non-preferential
Brg	Bearing
el	Element
FE	Finite element
fa	Flexible arm
fe	Flexible element
i	Inner
m	Membrane
max	Maximum
o	Outer
P	Polar
Rot	Rotor
r	Radial
T	Transverse
t	Tilting

Acronyms

BERM	Base excitation resonant mass
FEM	Finite element method
FD	Friction disk
FFT	Fast-Fourier-Transformation
HGJB	Herring-bone grooved journal bearing
ID	Inner diameter
MS	Membrane stack
OD	Outer diameter
Sil	Silicone coating

Tables

Table 1: Geometrical properties of investigated flexible membrane designs

	Var28	Var45	Var20	Var23	Var8	Var19	Var6
Material	1.4310	AL6082	AL6082	1.4310	1.4310	AL6082	AL6082
t [mm]	0.9	1.0	1.0	0.9	0.9	0.9	1.5
w [mm]	0.74	0.65	0.67	0.524	0.68	0.6	0.86
R_i [mm]	11.5	11.5	11.5	9.0	9.0	9.0	9.0
R_o [mm]	17.5	17.5	17.5	17.5	17.5	17.5	17.5
n_{fa} [-]	6	11	6	7	5	7	7

Table 2: List of instrumentation for dynamic characterization of flexible support and performance verification in the prototype.

Device	**Model**
Displacement probes	Lion precision C3S
Signal amplifier	Lion Precision CPL290
DAQ system	NI PXIe-1078/6356
Electrodynamic Shaker	Labworks INC. ET-139
Analog amplifier	Labworks INC. PA-138-1
Waveform generator	Agilent 33500B-Series

Table 3: Rotor design parameters

Bearing diameter D_{Brg}	10 mm
Bearing length-to-diameter ratio L_{Brg}/D_{Brg}	1
Rotor mass m_{Rot}	0.0289 kg
Polar rotor inertia J_P	4.3258e-07 kgm^2
Transverse rotor inertia J_T	1.8112e-05 kgm^2
Bearing distance l	58.5 mm
Nominal rotor speed N_{Rot}	250 krpm

Table 4: Range of design variables for the performed Monte-Carlo simulations

Material: Steel/aluminum/PEEK
Thickness t, width $w \in [0.3, 2]$ mm
Inner radius $R_i \in [8, 30]$ mm
Outer radius $R_o \in [8, 30]$ mm
Sector angle $\varphi \in [\pi/30, \pi/2]$
Number of annular sections $n_{as} \in [2, 6]$
Number of flexible arms $n_{fa} \in [4, 12]$
Number of finite elements per arm $n_{FE} = 20$

Table 5: Radial stiffness k_r and tilting stiffness k_t obtained with the parametric membrane model compared to results from 1D FE and 3D FE models

Method	k_r and deviation from (2)	k_t and deviation from (2)
(1) Membrane model	1.067e+06 N/m (-0.19%)	9.641 Nm/rad (+0.12%)
(2) FEM 1D	1.069e+06 N/m	9.629 Nm/rad
(3) FEM 3D	1.167e+06 N/m (+9.17%)	9.999 Nm/rad (+3.84%)

List of Figures

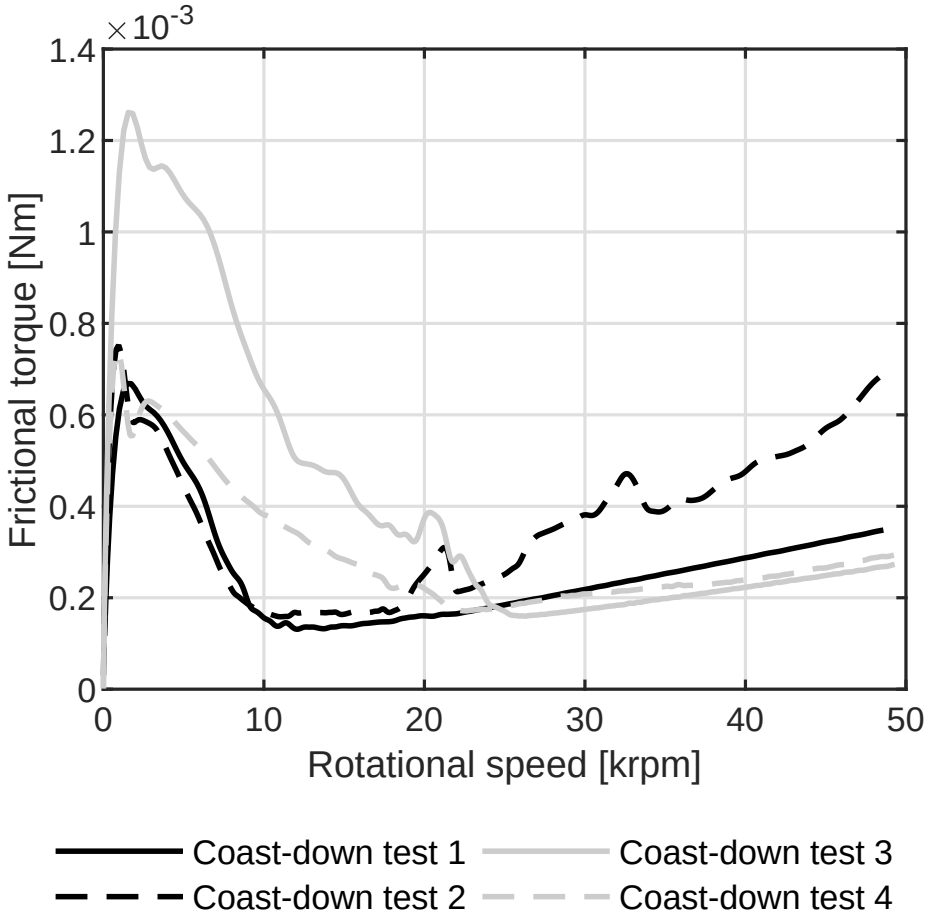

Figure 1: Coast-down frictional torque measurement results of O-Ring supported HGJB bushings

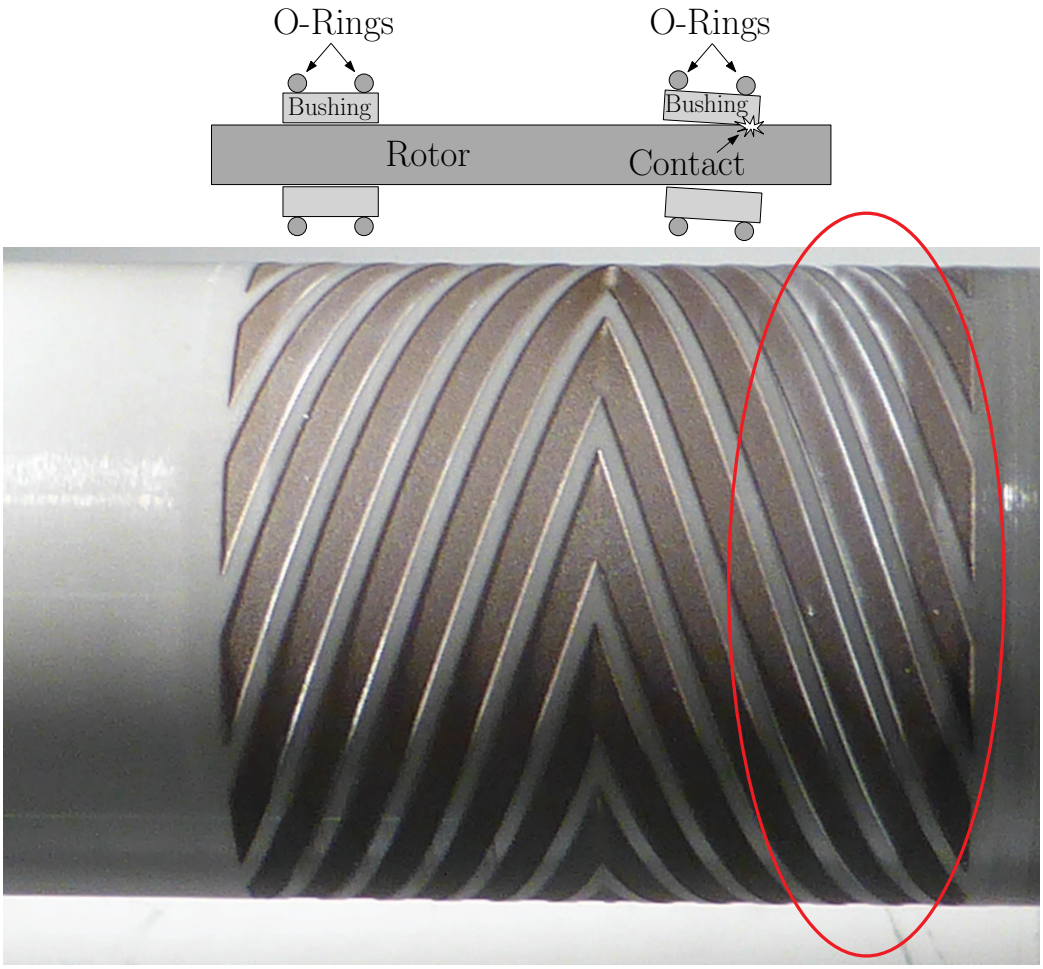

Figure 2: Wear on HGJB due to misalignment, visible by the accumulation of white dust in the bearing grooves of a silicone-nitride rotor shaft

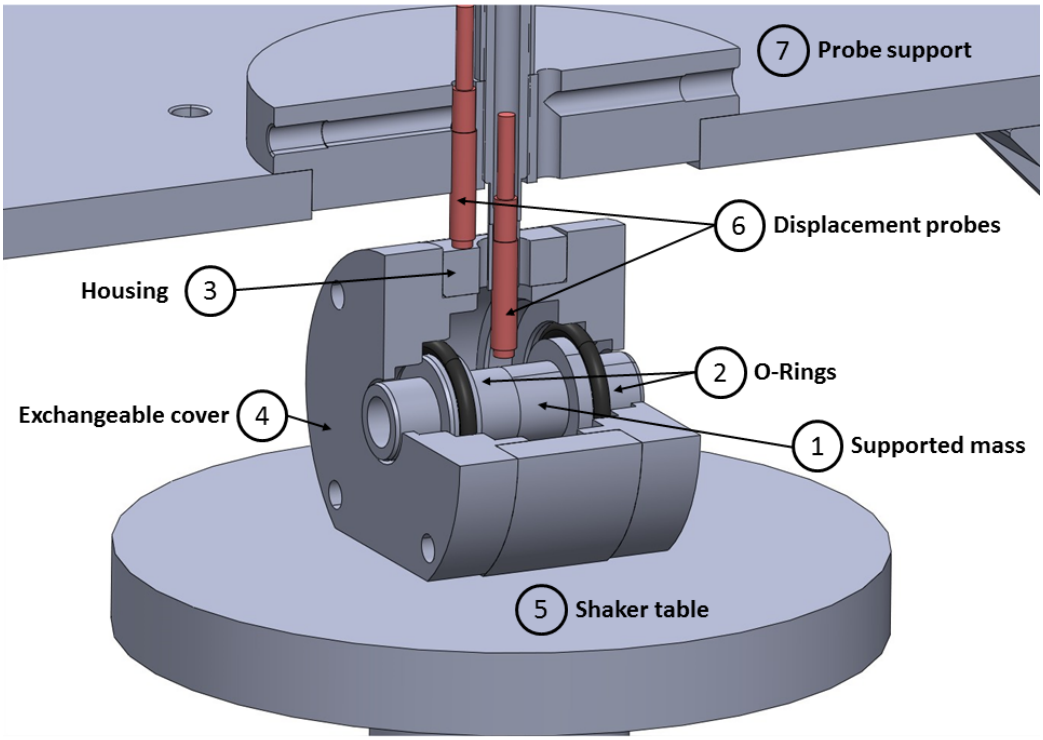

Figure 3: O-Ring test section with displacement probes

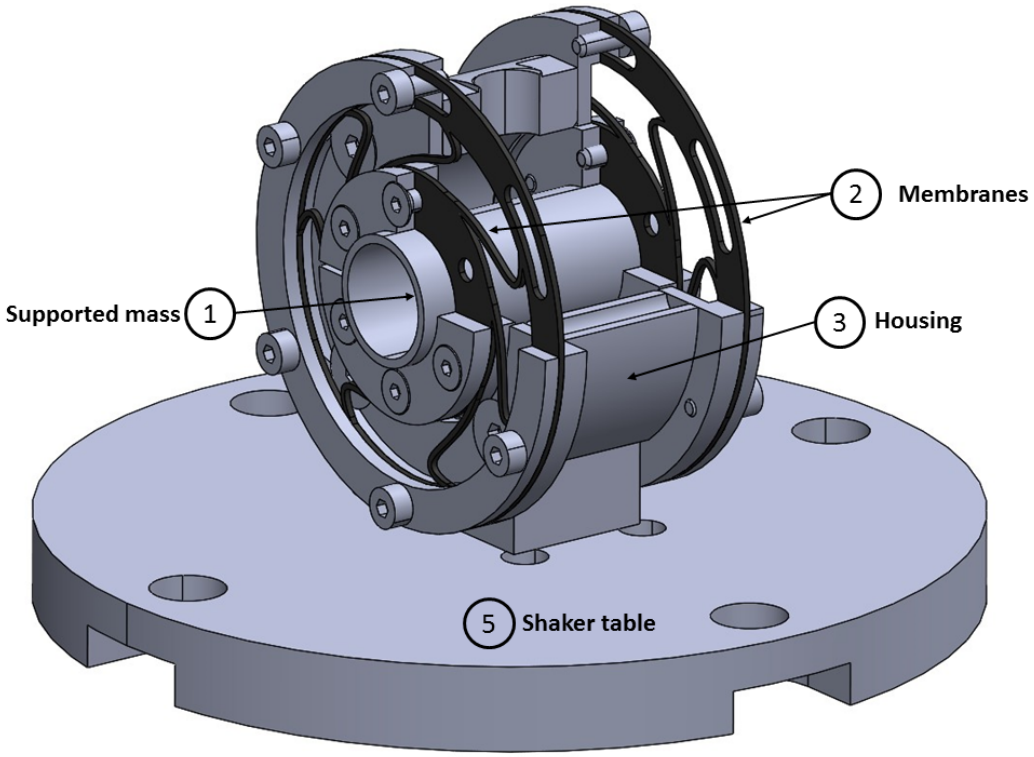

Figure 4: Membrane test section

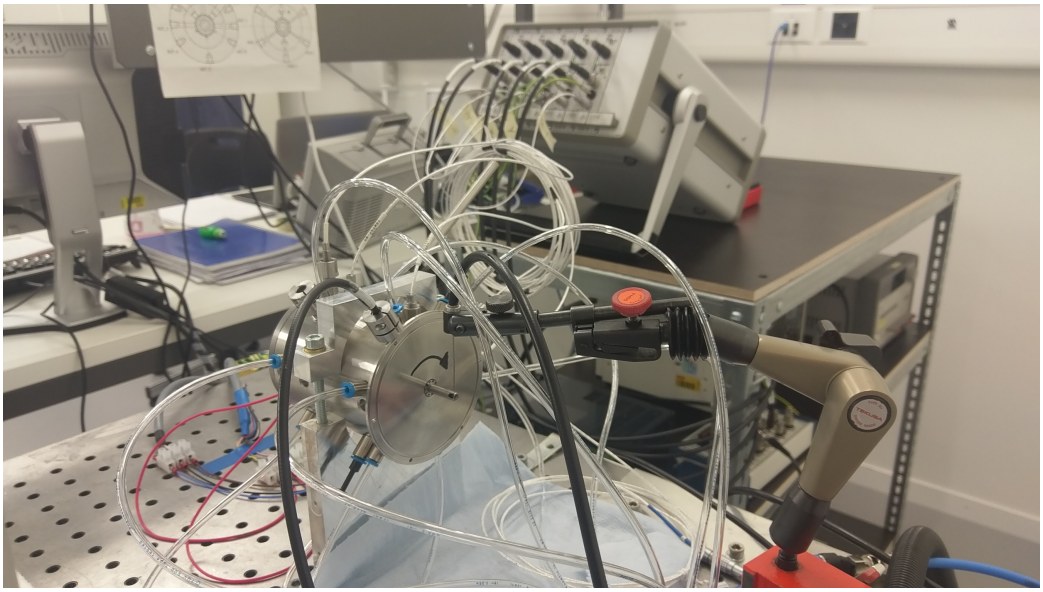

Figure 5: Prototype with implemented flexible membrane bushing support and instrumentation

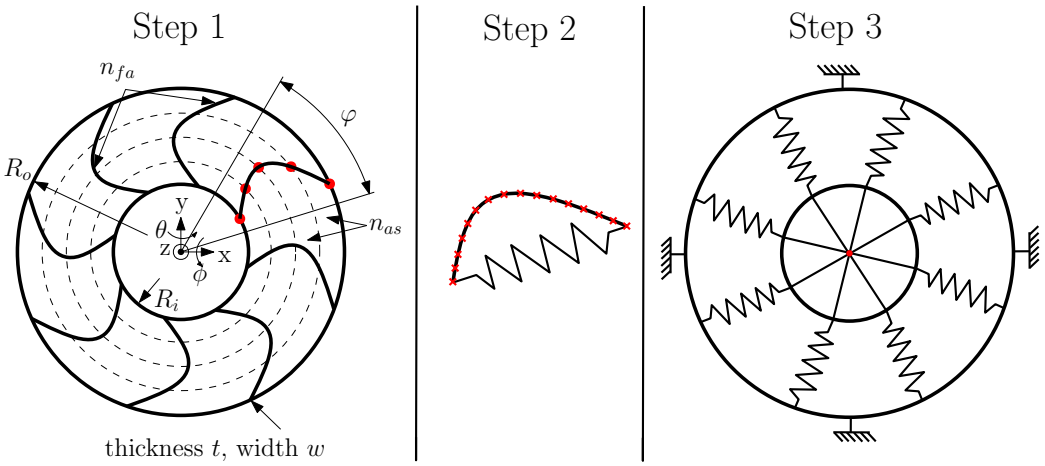

Figure 6: Available parameters of membrane model for calculating radial and tilting stiffness

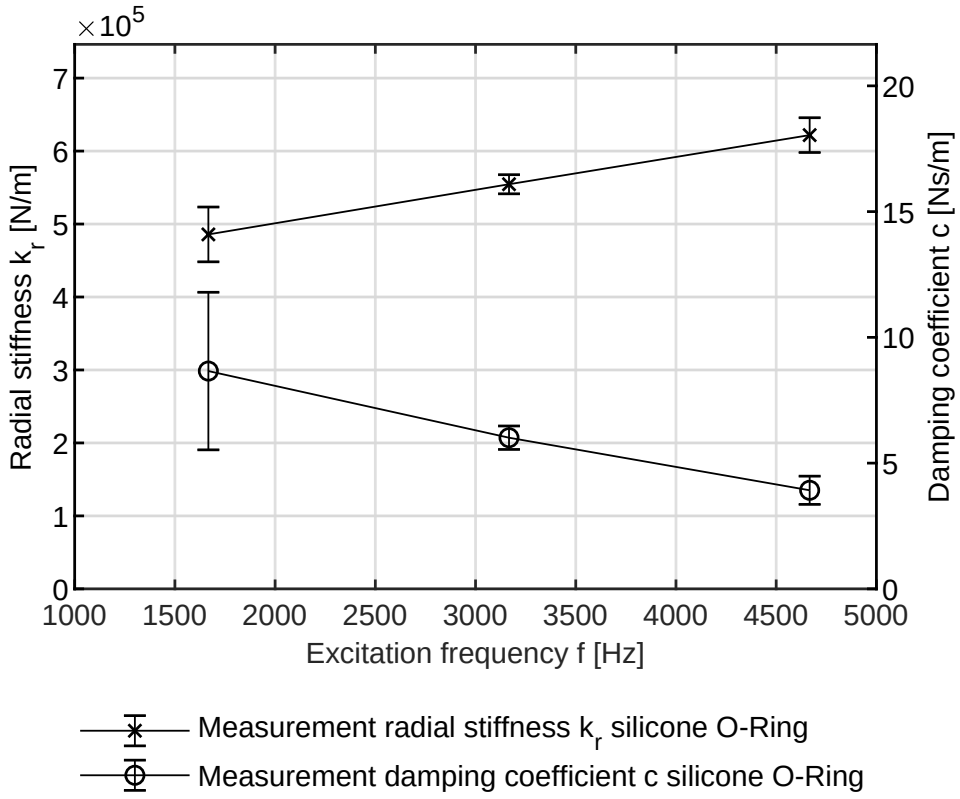

Figure 7: Results of stiffness and damping measurements of a single silicone O-Ring using the measurement setup presented in Fig.3

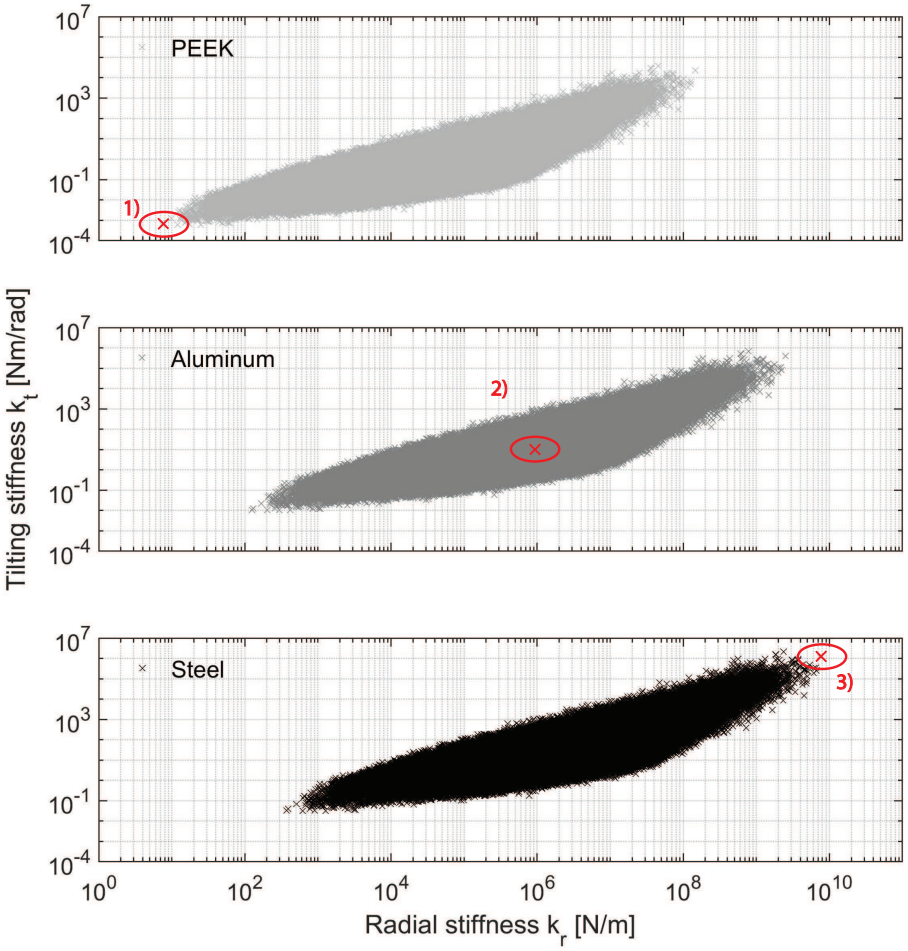

Figure 8: Results of 500000 Monte-Carlo simulations for PEEK, aluminum and steel membranes according the design variables in Tab.4

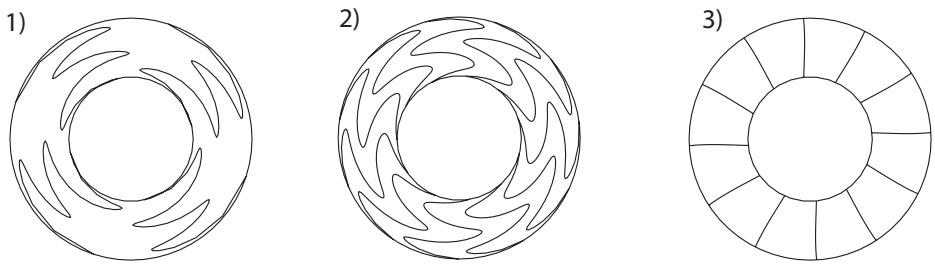

Figure 9: Three selected results in design space for low, intermediate and high stiffness

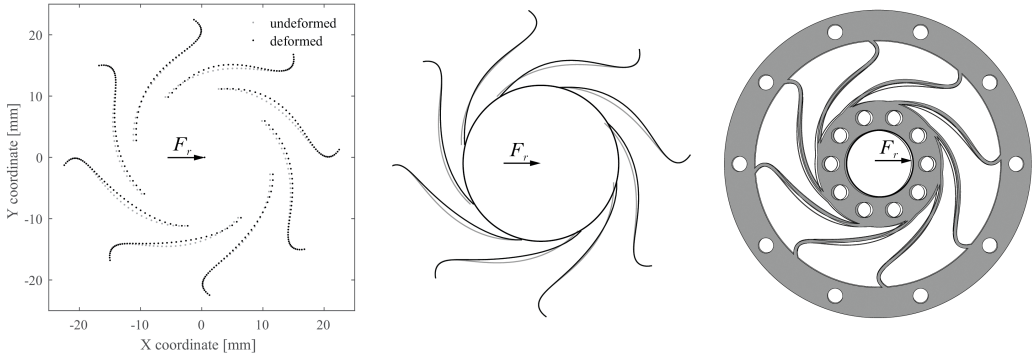

Figure 10: Comparison of displacement due to a radial force of 1 N in x-direction from parametric membrane model (left) with 1D FEM (middle) and 3D FEM results (right) (displacements scaled x500).

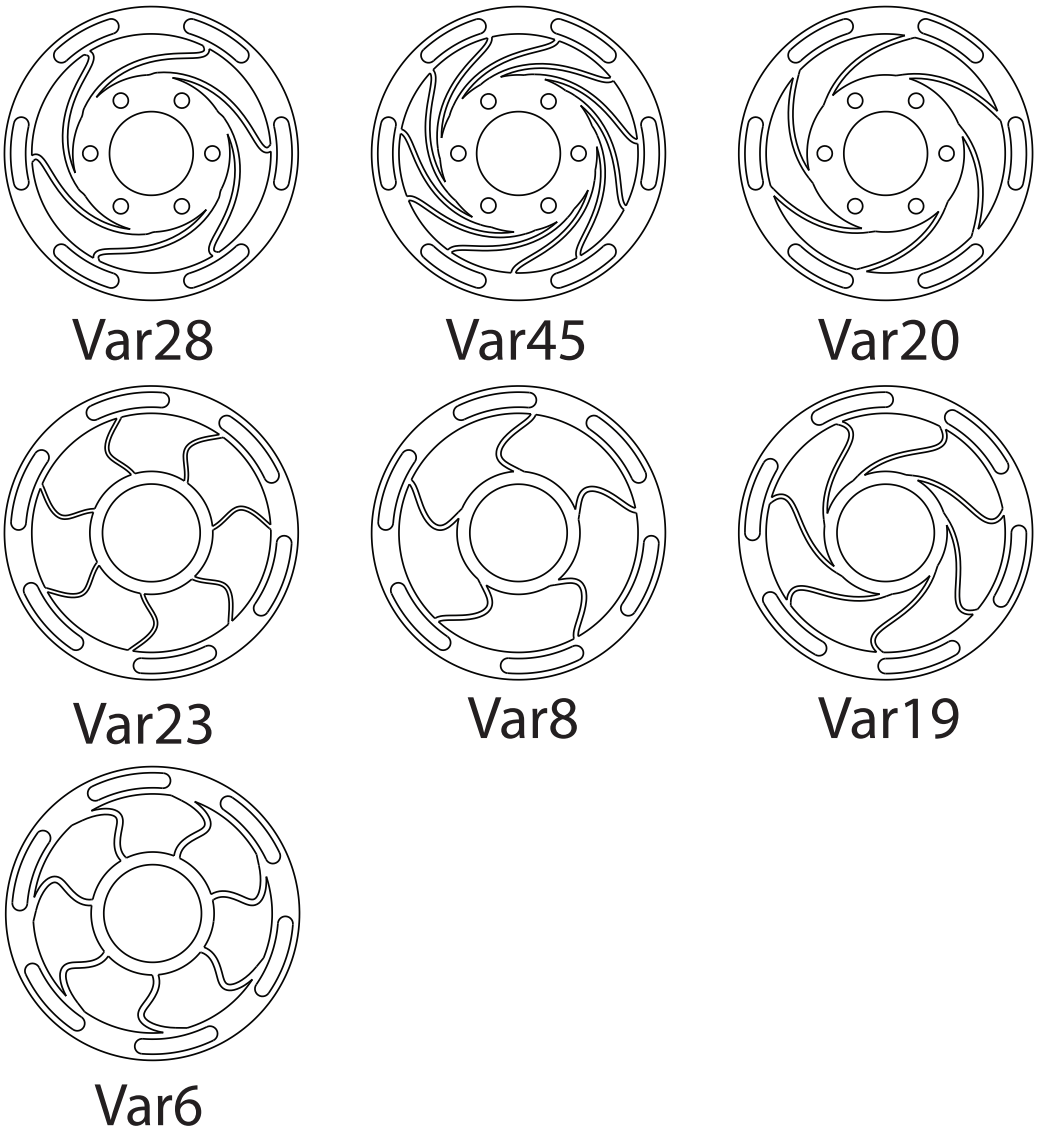

Figure 11: Overview of investigated membrane designs

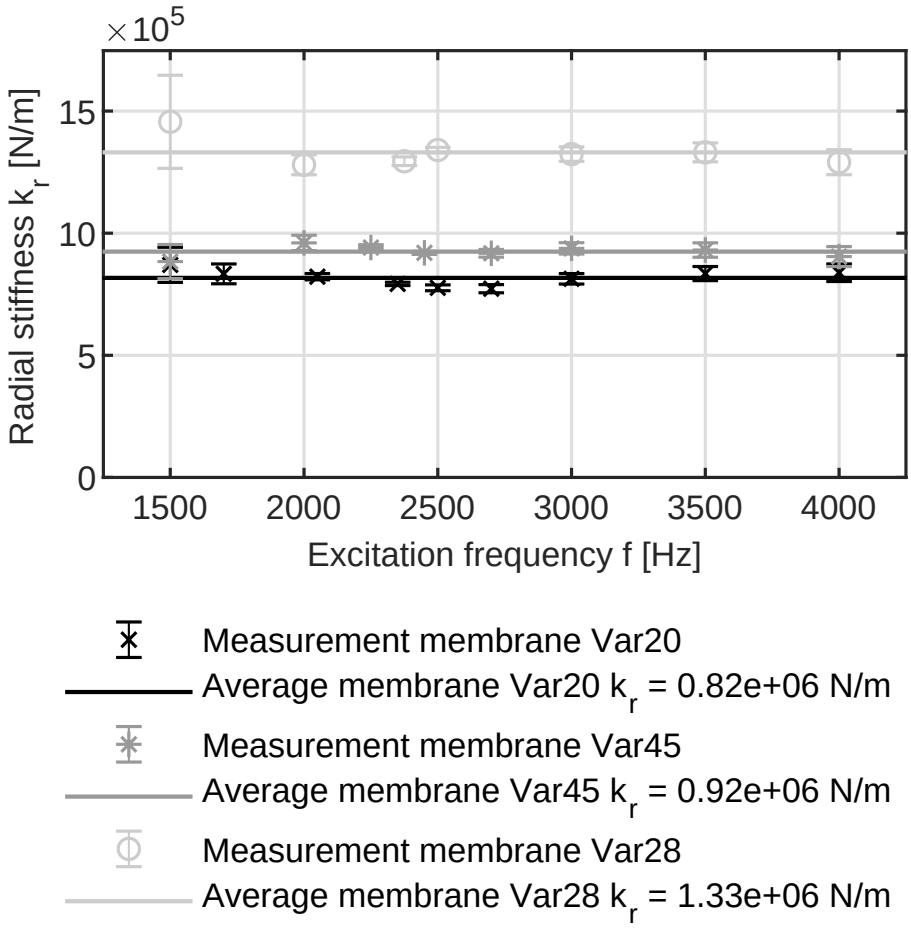

Figure 12: Measurement of radial stiffness k_r for aluminum membrane Var20 and Var45 and steel membrane Var28 using the base excitation-resonant mass method

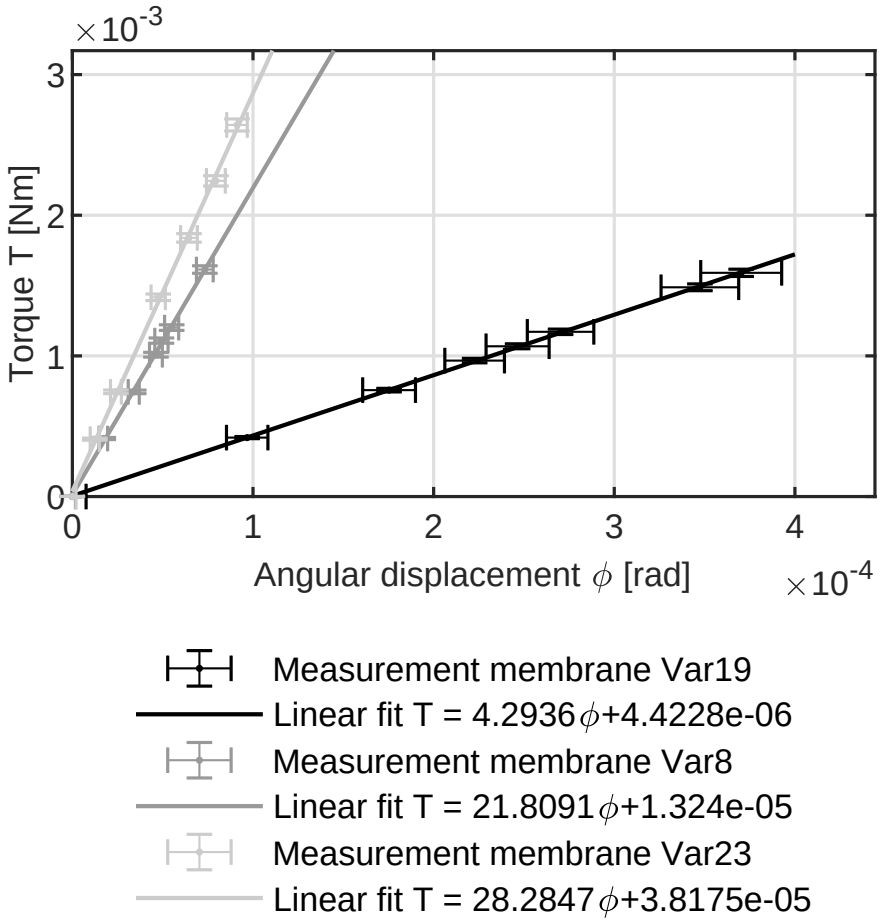

Figure 13: Measurement of tilting stiffness k_t for aluminum membrane Var19 and steel membranes Var8 and Var23

Figure 14: Overlay of designed geometry in CAD and real geometry of membrane Var23 achieved by laser cutting

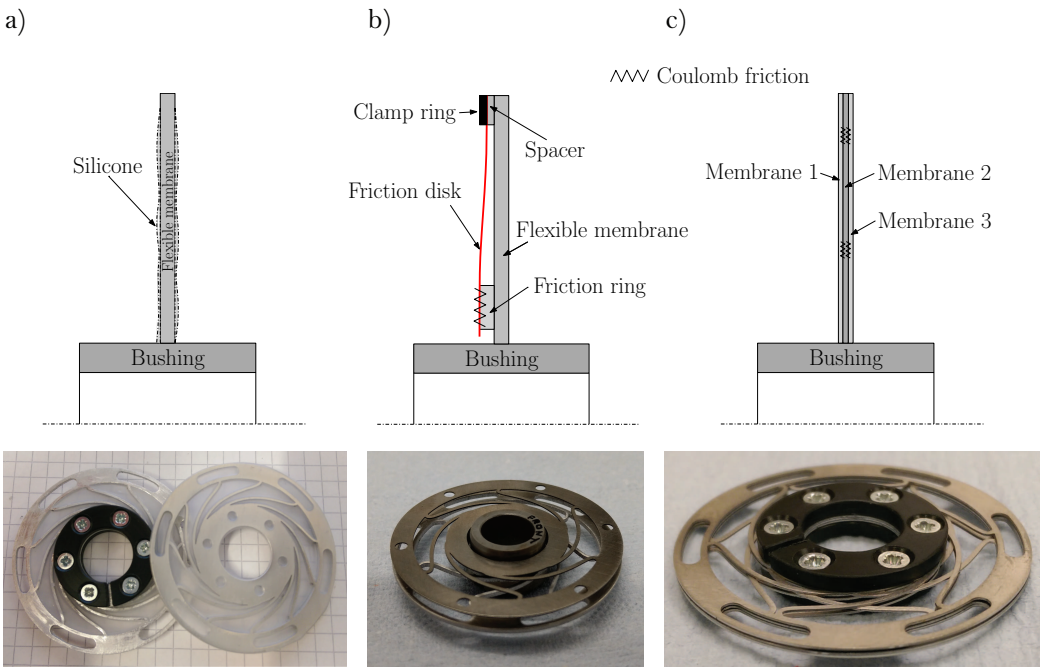

Figure 15: Damping concepts a) Silicone coating (Sil) b) Friction disk (FD) and c) Membrane stack (MS)

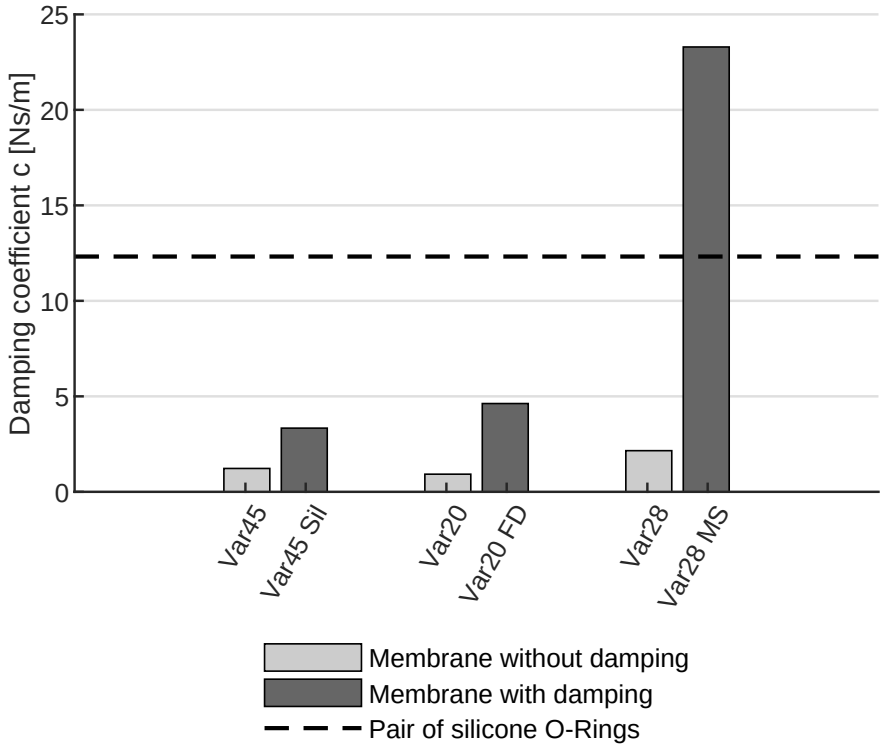

Figure 16: Comparison of damping coefficient c for aluminum membrane Var45 and Var20 and steel membrane Var28 in combination with the investigated damping concepts silicone coating (Sil), friction disk (FD) and membrane stack(MS)

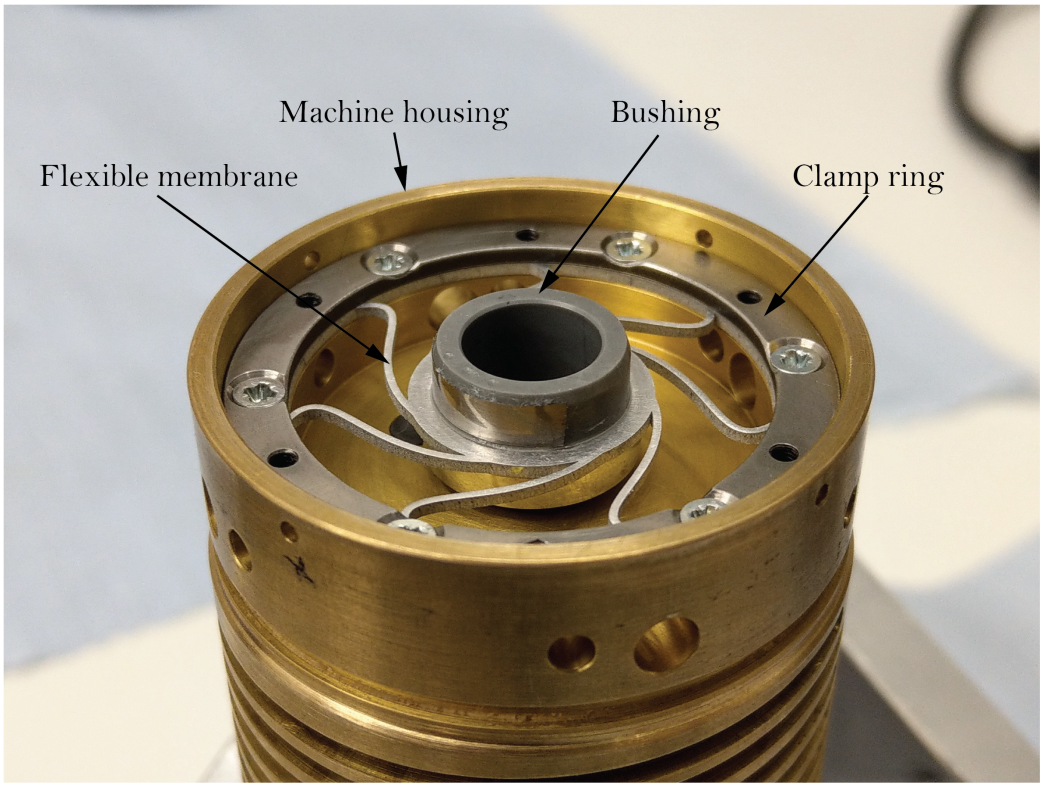

Figure 17: Aligned and glued bearing bushing supported on flexible membrane and fitted to the main housing by means of a clamp ring and bolts

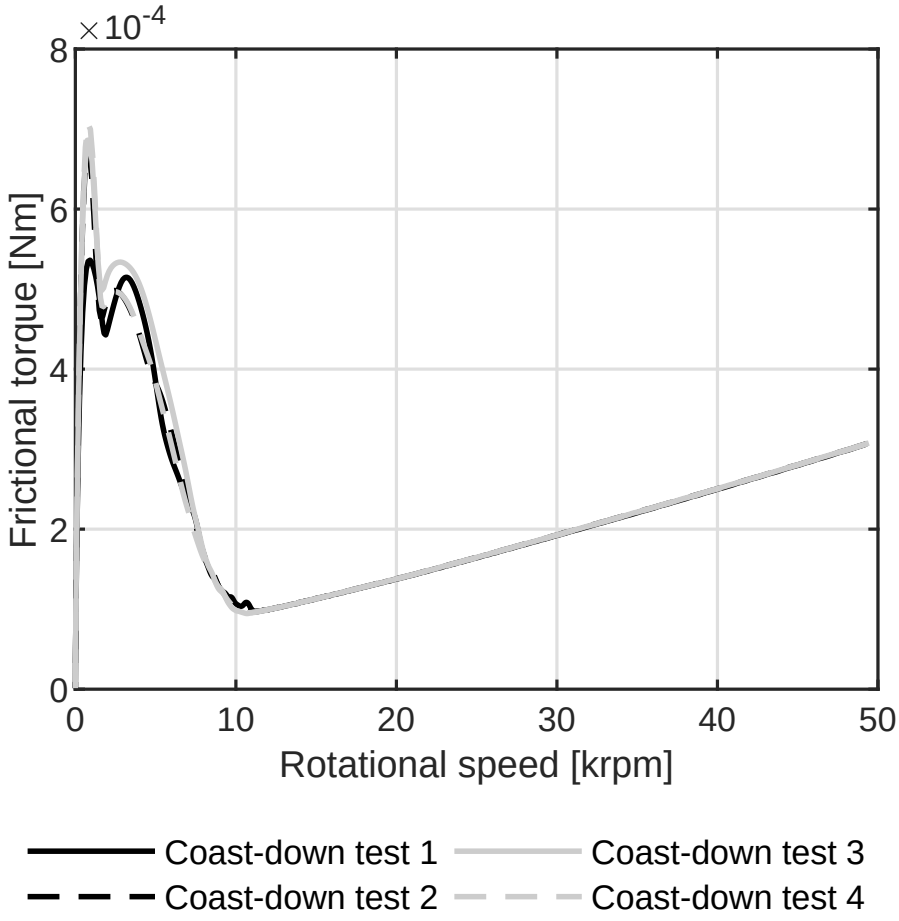

Figure 18: Coast-down measurement results of HGJB bushings supported on flexible membrane

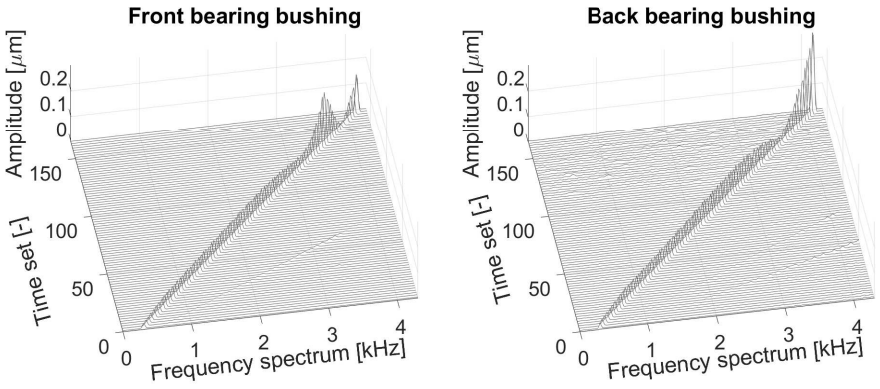

Figure 19: Waterfall plots of front and back bearing bushings supported on flexible membranes during speed ramp up to 250krpm

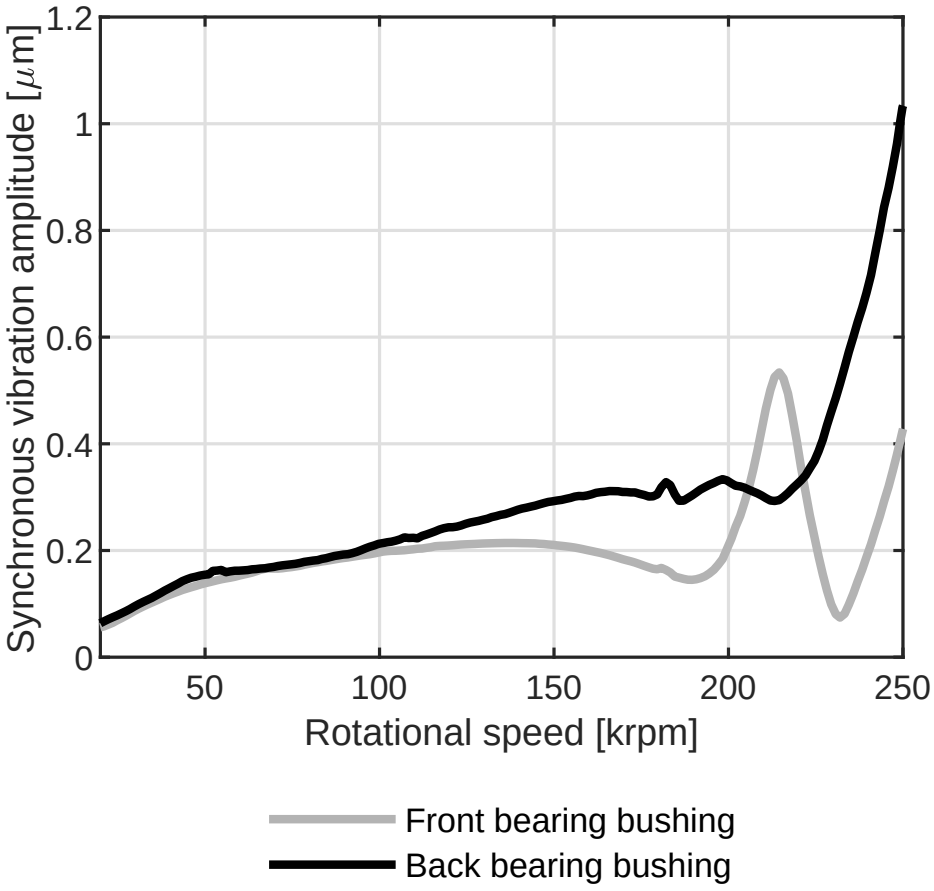

Figure 20: Synchronous vibration amplitude of front and back bearing bushings supported on flexible membranes during speed ramp up to 250 krpm